

Large Twist Angle dependent Ultrafast Transient Dynamics and Raman studies on MoSe₂/WSe₂ van der Waals Heterostructures

Vikas Arora^{1,2}, Pramoda K Nayak^{3,4}, Victor S Muthu¹, A K Sood^{*1,2}

November 27, 2024

¹*Department of Physics, Indian Institute of Science, Bangalore 560012, India*

²*Centre for Ultrafast Laser Applications, Indian Institute of Science, Bangalore 560012, India*

³*2D Materials Research and Innovation Group, Department of Physics, Indian Institute of Technology
Madras, Chennai 600036, India*

⁴*Centre for Nano and Materials Sciences, Jain (Deemed-to-be University), Jain Global Campus,
Kanakpura, Bangalore 562112, Karnataka, India*

Keywords: van der Waals Heterostructure, Raman spectroscopy, optical pump-optical probe spectroscopy, ultrafast carrier relaxation dynamics, interlayer excitons.

Abstract

Two-dimensional van der Waals heterostructures (HS) exhibit twist-angle (θ) dependent interlayer charge transfer, driven by moiré potential that tunes the electronic band structure with varying θ . Apart from the magic angles of $\sim 3^\circ$ and $\sim 57.5^\circ$ that show flat valence bands (twisted WSe₂ bilayer), the commensurate angles of 21.8° and 38.2° reveal the Umklapp light coupling of interlayer excitons (twisted MoSe₂/WSe₂ HS). We report a non-degenerate optical pump-optical probe spectroscopy and Raman spectroscopy of MoSe₂/WSe₂ HS at large twist angles. The recombination time of interlayer excitons reaches a minima near commensurate angles. Raman spectroscopy reveals an opposite shift in the A_{1g} modes of MoSe₂ and WSe₂, with the maximum shift occurring in the vicinity of twist angles of 21.8° and 38.2° . At these commensurate angles, maximum charge transfer increases Coulomb screening, reducing the interlayer exciton lifetime. This study emphasizes

the significance of the large twist angle of HS in developing transition metal dichalcogenides-based optoelectronic devices.

Introduction

Two-dimensional materials such as graphene, transition metal dichalcogenides (TMDs), and h-BN, along with their heterostructures (HS), show many exciting physical properties. For example, in the case of TMDs, properties such as the large binding energy of excitons [1–3], a strong non-linear optical response [4–6] and spin-valley coupling [7, 8] are exhibited. For the heterobilayers MoX_2/WX_2 , the energy levels are decided by d orbitals of transition metal. The $5d$ orbital of W is higher than that of the $4d$ orbital of Mo, and hence, the conduction band minima and valence band maxima of Tungsten are higher than that of Molybdenum. This creates a staggered or type-II band alignment [9, 10]. This alignment facilitates ultrafast charge transfer between the layers, generation of interlayer exciton with longer decay times [11, 12], and energy transfer among the layers [3, 13]. The optoelectronic properties have been shown to depend on the twist angle between the layers. The twist between the two layers gives rise to a periodic array of potential minima known as the moiré pattern [14–17]. At low temperatures and low twist angles, the multiple sharp peaks superimposed over the photoluminescence (PL) spectra denotes the interlayer excitons trapped in moiré quantum wells [18, 19]. For $\text{WSe}_2/\text{MoSe}_2$ HS, excitons trapped by the moiré potential become free interlayer excitons at temperatures above 100 K, as indicated by the sign reversal of the excitonic magnetic moment [20]. The width of moiré potential decreases as the twist angle is enhanced [18]. Self-organized quantum dots are observed in $\text{MoSe}_2/\text{WSe}_2$ and MoS_2/WS_2 HS for twist angles less than 0.5° [21]. For $\text{WS}_2/\text{MoSe}_2$ HS, twist tunes the moiré reciprocal lattice and hence the properties of moiré excitons such as oscillator strength and inter/intralayer mixing [22]. In a twisted WSe_2 bilayer, flat top moiré valence bands are observed at magic angles of $\sim 3^\circ$ and $\sim 57.5^\circ$ [23, 24]. While small twist angles reveal the properties of moiré excitons, large twist angles describe the characteristics of interlayer excitons.

Nayak *et al.* [10] observed the quenching of photoluminescence for the $\text{MoSe}_2/\text{WSe}_2$ HS for all the twist angles as compared to constituent monolayers but, with a slight variation in redshift depending on the twist angle [25]. It has been reported that the PL is two orders lesser for $\theta = 20^\circ$ as compared to $\theta = 2^\circ$ for $\text{MoSe}_2/\text{WSe}_2$ HS [26]. Intriguingly, other PL studies reveal that at all non-zero twist angles, the momentum-direct interlayer excitons in $\text{MoSe}_2/\text{WSe}_2$ (K-K exciton) HS exhibit a red-shift [27]

whereas the momentum-indirect interlayer excitons (Γ -K exciton) in $\text{MoSe}_2/\text{MoS}_2$ HS show a blue shift, indicating strong dehybridization [28]. The interlayer distance and binding energy of interlayer exciton are twist-dependent and are maximum at 30° , as revealed by the PL studies [29, 30]. Yu H. *et al.* have shown that the interlayer excitons undergo Umklapp recombination near the commensurate twist angles of 21.8° and 38.2° [26, 31]. The additional channel for recombination of interlayer excitons at these particular angles predicts anomalous relaxation dynamics for the HS. The significance of the commensurate angle 21.8° has been emphasized in recent reports on HS $\text{MoS}_2/\text{MoSe}_2$, demonstrating the highest thermoelectric performance ($ZT = 2.96$ at $T = 700$ K) [32] and recording the highest indirect bandgap [33].

Using Raman spectroscopy, Wu *et al.* [30] observed the opposite shifts of out-of-plane A_{1g} modes of MoS_2 and WS_2 with the twist angle due to altered electron density in constituent layers of HS MoS_2/WS_2 . Using polarized low-frequency Raman spectroscopy of twisted HS $\text{WSe}_2/\text{MoSe}_2$ and MoS_2/WS_2 , layer breathing (LB) and layer shear (LS) modes show twist-dependence and LB mode disappears at intermediate twist angles [34, 35]. A recent report on ultrafast electron diffraction of $\text{MoSe}_2/\text{WSe}_2$ HS indicates that interlayer heat transfer occurs on a ~ 20 ps timescale, mediated by nonthermal phonons followed by interlayer charge transfer and scattering [36]. The ultrafast transient absorption spectroscopy of TMDs HS has shown that the interlayer charge transfer happens on the order of 100 fs time scale [37–42]. A slight variation in geometry or twist of the HS can vary the charge transfer time from 100 fs to 1 ps [3, 35, 43]. There have been many reports on the different HSs for carrier relaxation dynamics, but only for small twist angles [35, 43, 44]. To the best of our knowledge, there is no systematic study of carrier relaxation dynamics for large twist angles in the TMD HS.

Here, we report the non-degenerate optical pump-optical probe studies of $\text{MoSe}_2/\text{WSe}_2$ HS at different twist angles at ambient conditions. A significant decrease in the decay time of interlayer excitons near the commensurate angles of 21.8° and 38.2° is observed, attributed to Umklapp recombination. Our Raman spectra of this HS at different twist angles show out-of-plane (A_{1g}) modes of constituent monolayers of the HS shifting in the opposite direction as the twist angle is varied. The shift is maximum in the vicinity of the commensurate angles. We also observed the disappearance of longitudinal acoustic mode (2LA) of WSe_2 in the proximity of commensurate angles. Our present study paves the way towards the application of type-II HSs in designing optoelectronic devices, namely photovoltaics, photodetectors, and light-emitting devices where charge transfer and recombination times are important parameters [45].

Experimental details

Non-generate optical pump-optical probe measurements were performed using Ti: Sapphire ultrafast laser system (1 kHz repetition rate, \sim 50 fs pulse width, M/s Spectra-Physics, Spitfire Ace) with the pump and probe energies of 3.1 eV and 1.55 eV, respectively. The pump and probe beams are passed collinearly through an objective lens with the NA = 0.9. The spot size of the beam at the sample point was measured to be \sim 5 μ m. Experiments were carried out at two pump fluences of 2.0 and 2.8 mJ/cm² at room temperature. The unpolarized Raman Spectroscopy was performed in backscattering geometry using a continuous laser of wavelength 532 nm and energy \sim 1 mW using an objective lens of 100x magnification. The experiments were performed for different twist angles of MoSe₂/WSe₂ HS.

The MoSe₂/WSe₂ HS was prepared using the chemical vapor deposition method on a *c*-plane sapphire substrate via a two-step process similar to our earlier work [10]. The individual monolayers of MoSe₂ and WSe₂ have a triangular geometry as shown in the microscopic image of the sample (Figure 1a). The triangles with light (bright) contrast and bigger (smaller) in size represent WSe₂ (MoSe₂) monolayers as depicted by the black arrows in Figure 1a. A random alignment of triangular-shaped monolayers was obtained as a result of the CVD process, providing us with various twist angles. It has been verified that the TMDs with triangular geometry terminate with transition metal atoms at the edges using transmission electron microscopy [46] and scanning tunneling microscopy [47]. Therefore, the relative orientation of the layers provides us with the angle between the two layers as there is a direct correlation of crystal orientation with the triangular geometry of each monolayer [35, 46, 48]. The twist angle is evaluated as the angle between two lines collinear to the centroid and the vertex of the triangle [49]. One example of evaluating the twist angle is presented in Figure 1b, where red and blue outlined triangles represent MoSe₂ and WSe₂ monolayers, respectively. The lines collinear to the vertex and centroid are the angle bisector in the case of equilateral triangles, which gives the twist angle. The schemes for the front and side view of MoSe₂/WSe₂ HS for different twist angles are shown elsewhere [10]. Figure 1c shows the Raman spectrum of the HS region for a twist angle of 49°. It confirms the formation of HS with the presence of all the modes of individual monolayers of MoSe₂ and WSe₂, described later in the work.

Results and discussions

1 Optical pump - optical probe studies

Figure 2 shows the type II band alignment in MoSe₂/WSe₂ HS depicting higher energy states of valence band maxima (VBM) and conduction band minima (CBM) of WSe₂ with respect to that of MoSe₂. The optical pump excitation using 400 nm (3.1 eV) laser pulse injects carriers in the conduction band much above the band gap of the constituent monolayers (MoSe₂ E_g=1.57 eV, WSe₂ E_g=1.67 eV) [50,51]. The energetic hot carriers undergo rapid electron-electron scattering, relax down to the band edge, and create inter and intralayer excitons [37,38]. These excitons come into the picture after a few hundred femtoseconds after the photoexcitation, when most of the electrons (holes) get transferred to CBM (VBM) of MoSe₂ (WSe₂) as shown in Figure 2 [38,39]. The interlayer exciton takes a longer time to recombine as the electron and holes are in different layers in comparison to intralayer excitons. The relative change in the reflectivity $\Delta R/R$ is recorded as a function of delay time between pump and probe beams at room temperature for different twist angles of HS, as shown in Figure 3a & 3b. We observed the biexponential decay for the excited carriers. We normalize the time-resolved data after subtracting the constant term after ~ 100 ps (Figure 3a), which represents the residual thermal processes that take hundreds of picoseconds to a few nanoseconds to relax. To determine these decay times, we used the following relaxation dynamics model:

$$\frac{\Delta R}{R(t)} = \frac{1}{2}(1 + \text{erf}(\frac{t - t_0}{\tau_r}))(A_1 e^{-t/\tau_1} + (1 - A_1)e^{-t/\tau_2}) \quad (1)$$

where A_1 and $(1 - A_1)$ represent the fraction of photoexcited carriers that formed intralayer and interlayer exciton density, respectively. The red solid line in Figure 3a represents the fit obtained in Eq 1. The normalized $\Delta R(t)/R$ for the different twist angles at a fluence of 2.0 mJ/cm² is shown in Figure 3b. The graph clearly depicts the twist dependence of relaxation time τ_2 , whereas τ_1 is independent of θ . The fast decay time $\tau_1 \sim 8$ ps is due to the recombination time of intralayer excitons, and $\tau_2 \sim 45$ ps is the recombination time for interlayer excitons [52,53].

Figure 3c shows the θ -dependent behavior of the fraction of interlayer exciton density $(1 - A_1)$ and its recombination time τ_2 at two different fluences of 2.0 mJ/cm² and 2.8 mJ/cm². We do not observe any systematic behavior of $(1 - A_1)$ with different twist angles. However, we observe that it is smaller at higher fluence, as shown in the shaded region of Figure 3c. This illustrates that with the increased fluence, there is a slight increase in interlayer exciton density, but the intralayer exciton density increases

significantly. It is represented by the ratio of amplitudes A_1 and $1-A_1$, which increases with an increase in fluence for all twist angles (top panel of Figure 3d). We can conclude that an increase in fluence leads to saturation of the interlayer charge transfer, consequently increasing the density of intralayer excitons. For both the pump fluences, the recombination time of interlayer excitons τ_2 (Figure 3c), τ_2 is independent of $\theta < 19^\circ$, followed by the minimum at $\sim 23^\circ$ and $\sim 38^\circ$. The blue dots and red triangles represent the data for the two given fluences, whereas a solid blue line represents a guide to the eye.

We offer a qualitative understanding of our results. We observed that τ_2 is maximum at the twist angle of 30° , *i.e.* the interlayer excitons take the longest time to recombine. This is due to the interlayer distance being maximum at the twist angle of 30° in TMDs HSs [29, 30]. Equally interesting is the observation of two minima of τ_2 observed in the range of 20° - 25° and 35 - 38° . These two ranges of twist angles cover the commensurate angles of $\theta = 21.8^\circ$ and 38.2° for MoSe₂/WSe₂ HS, where interlayer excitons can access an additional channel to recombine [26, 31]. *Seyler et al.* have demonstrated that for any non-zero twist angle between two layers, the holes in the valence band of WSe₂ and electrons in the conduction band of MoSe₂ at $\pm K$ points do not align in the first Brillouin zone. However, at the commensurate angle of 21.8° , the valence band and conduction band align at $\pm K$ points in the second Brillouin zone, as shown in Figure 4, adapted from ref. [26]. These excitons can recombine radiatively, and the momentum mismatch (due to non-zero twist) is compensated by the reciprocal lattice of two layers; the process known as Umklapp recombination [26, 31]. We attribute this Umklapp recombination in the vicinity of commensurate angles of 21.8° and 38.2° as a cause for the anomalous minima of τ_2 . The two different fluences support the evidence of anomaly of relaxation dynamics in the vicinity of commensurate twist angles. Although the fraction of intralayer excitons increases with an increase in fluence (Figure 3d), the absolute numbers of interlayer and intralayer excitons increase with an increase in the fluence across all twist angles. This increment in the number of interlayer excitons results in longer recombination time as fluence increases (lower panel of Figure 3d). The fluence dependence at 20° , near the commensurate angles, displays that with the increase in fluence, there is no significant increase in the fraction of intralayer to interlayer excitons ($A_1/(1-A_1)$), suggesting that both types of excitons increase proportionally. It is important to note that the τ_2 value remains approximately constant at 20° with increasing fluence, even after a significant increase in the number of interlayer excitons compared to other twist angles. In conclusion, additional recombination channels for interlayer excitons at commensurate angles enhance their saturation density and keep the recombination time (τ_2) independent of fluence within the reported range.

2 Twist angle dependent Raman studies in MoSe₂/WSe₂ HS

The blue and red shifts of the A_{1g} modes in WS₂ and MoS₂ within their twisted HSs [30] motivated us to perform Raman spectroscopy on HS MoSe₂/WSe₂ for various twist angles. The group theory for the individual layer provides the irreducible decomposition of Raman active vibration modes $A_{1g}(R)$, $E_{2g}(R)$, and E_{1g} (IR+R) for MX₂ monolayer [54]. For the HS, we obtain the following vibration modes as shown in Figure 1c: M1(MoSe₂, A_{1g}): 238.5 cm⁻¹, M2(WSe₂, A_{1g} + E_{2g}): 249 cm⁻¹, M3(WSe₂, 2LA): 258.5 cm⁻¹, M4(MoSe₂, E_{2g}): 286 cm⁻¹, M5(WSe₂, A''_2): 305 cm⁻¹, M6(MoSe₂, A''_2): 353 cm⁻¹, M7: 373 cm⁻¹ and M8: 394 cm⁻¹ [55, 56]. From the perspective of the charge transfer among two vertically stacked monolayers, we concentrate on the out-of-plane modes (A_{1g}) of the two monolayers MoSe₂ and WSe₂ stacked together, namely M1 (MoSe₂) and M2 (WSe₂).

Figure 5a shows the normalized intensities of M1, M2, and M3 with different twist angles. The black dashed lines represent the shift of the peak position of modes M1 or M2 at different twist angles. This systematic behavior of M1 and M2 can be seen in Figure 5b, where the dashed red lines (a guide to the eye) show the opposite slopes for M1 and M2 modes for four different ranges of the twist angles. We observed the softening of M1 and hardening of M2 mode for any non-zero twist as compared to the aligned geometry (depicted by blue circles for zero twist angle in Figure 5a). Mode M2 starts stiffening as the twist angle is varied till 17°, followed by softening till 32° and then stiffening again till 39° which is again followed by softening. In a counter behavior, the M1 mode softens as the twist angle is varied till 17°, followed by stiffening till 32° and then softening till 39°, which is again followed by stiffening. The softening and stiffening of the A_{1g} mode (both M1 and M2) depend upon the carrier doping as well as the interlayer coupling [49, 57, 58]. In transition metal dichalcogenide MoS₂, increasing the number of layers stiffens the A_{1g} mode and softens the E_{2g} mode due to increased dielectric screening of Coulomb interactions [59, 60]. It has been reported that the unidirectional transfer of electrons from monolayer WS₂ to monolayer MoS₂ leads to higher carrier density in MoS₂ and lower carrier density in WS₂, which can soften or stiffen the respective A_{1g} modes [30]. For the similar staggered bands configuration of HS MoSe₂/WSe₂, unidirectional electron flow from WSe₂ to MoSe₂ increases (reduces) the carrier density in MoSe₂ (WSe₂) and leads to the softening (stiffening) of M1 (M2) modes. To understand the importance of twist angle, we have plotted the difference between the peak position of modes M1 and M2 with twist angles as shown in Figure 5c. A guide to the eye (solid red curve) shows a systematic variation of the shift of M1 with respect to M2 (or vice-versa) with maximum shift near the commensurate angles of 21.8° and 38.2°. For perfectly aligned HS ($\theta=0^\circ$), the electron transfer and the interlayer coupling lead

to the softening of A_{1g} of both M1 and M2 modes, if we compare these modes in monolayers of MoSe₂ and WSe₂ (Figure 5a). However, with a non-zero twist angle, variation in the charge transfer and the interlayer coupling tunes the softening and the corresponding stiffening of M1 and M2 modes and shows an anomalous maximum shift at the angle of 19° and 39°. This can be understood as the maximum electron transfer and more dielectric screening of Coulomb interaction between electron and hole for the MoSe₂/WSe₂ HS at these specific angles, which are in the vicinity of commensurate angles. This anomalous behavior led us to observe the evolution of other modes of HS with twist angle.

The disappearance of M3 (2LA mode of WSe₂) at the twist angles of 19° and 39° as depicted by small arrows in Figure 5a (panel iii) is observed. Interestingly, this observation for M3 mode happens in the vicinity of commensurate angles 21.8° & 38.2° which needs further investigation. Thus, the characteristics of M1 and M2 modes provide us with strong evidence of maximum equilibrium charge transfer in the MoSe₂/WSe₂ HS at commensurate angles.

Optical pump-optical probe spectroscopy and Raman spectroscopy reveal that charge transfer between MoSe₂ and WSe₂ layers in the heterobilayer is maximum near commensurate angles of 21.8° and 38.2°. This increased charge transfer leads to more screening of Coulomb interactions between electrons and holes, resulting in a shorter lifetime for interlayer excitons. This decrease in τ_2 is also accompanied by the additional recombination channel provided by the Umklapp process.

Conclusions

In summary, we have reported the optical pump optical probe spectroscopy of MoSe₂/WSe₂ HS with different twist angles. We observed a significant decrease in interlayer exciton recombination time in the proximity of commensurate angles of 21.8° and 38.2°. We interpret the result as a consequence of the availability of new radiative recombination channels as a result of Umklapp recombination. Raman spectra show the systematic softening and stiffening of the A_{1g} modes M1 and M2 with the non-zero twist angle, a consequence of unidirectional charge transfer in TMDs with type-II band configuration. The maximum shift in modes M1 and M2 has been observed again in the vicinity of commensurate angles. Our results can be helpful in designing the applications of twisted vdW HS in optoelectronic applications.

Conflicts of interest

There are no conflicts of interest to declare.

Acknowledgments

AKS thanks the Department of Science and Technology for its financial support under the National Science Chair Professorship. VA acknowledges CSIR for the research fellowship. PKN acknowledges the MHRD STARS research grant [STARS/APR2019/396].

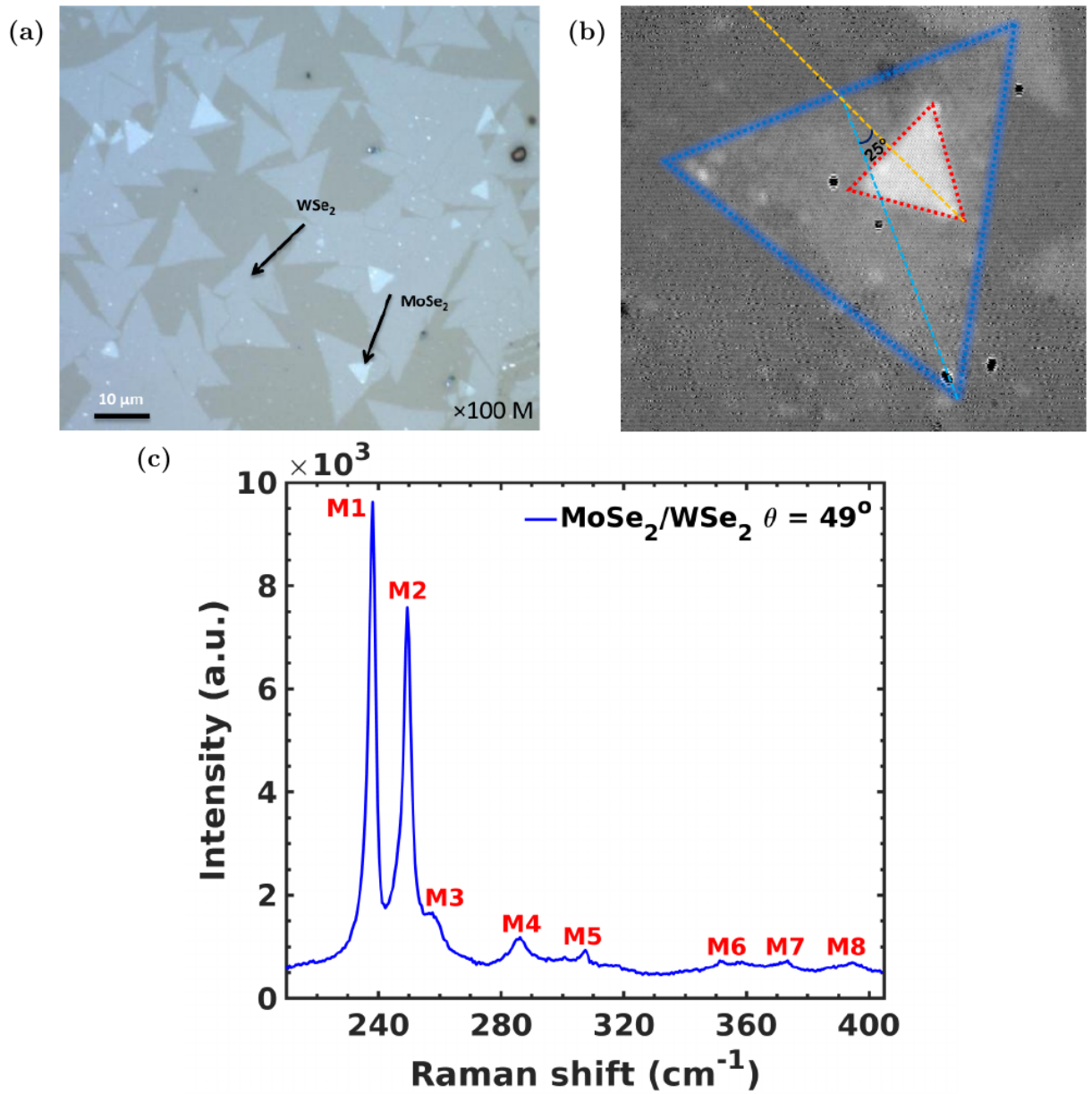


Figure 1: (a) Microscopic image of MoSe₂/WSe₂ HS depicting WSe₂ as a bottom layer (big triangles) with dull contrast and MoSe₂ as a top layer (smaller triangles) with brighter contrast, (b) Angle evaluation between two monolayers with the blue(red) triangle as a boundary of WSe₂(MoSe₂) monolayers, (c) The Raman spectrum for HS at a $\theta = 49^\circ$. M1(M2) represents the A_{1g} mode of MoSe₂(WSe₂), The respective modes are as follows: M1(238.5 cm^{-1}), M2(249 cm^{-1}), M3(258.5 cm^{-1}), M4(286 cm^{-1}), M5(305 cm^{-1}), M6(353 cm^{-1}), M7(373 cm^{-1}), M8(394 cm^{-1}).

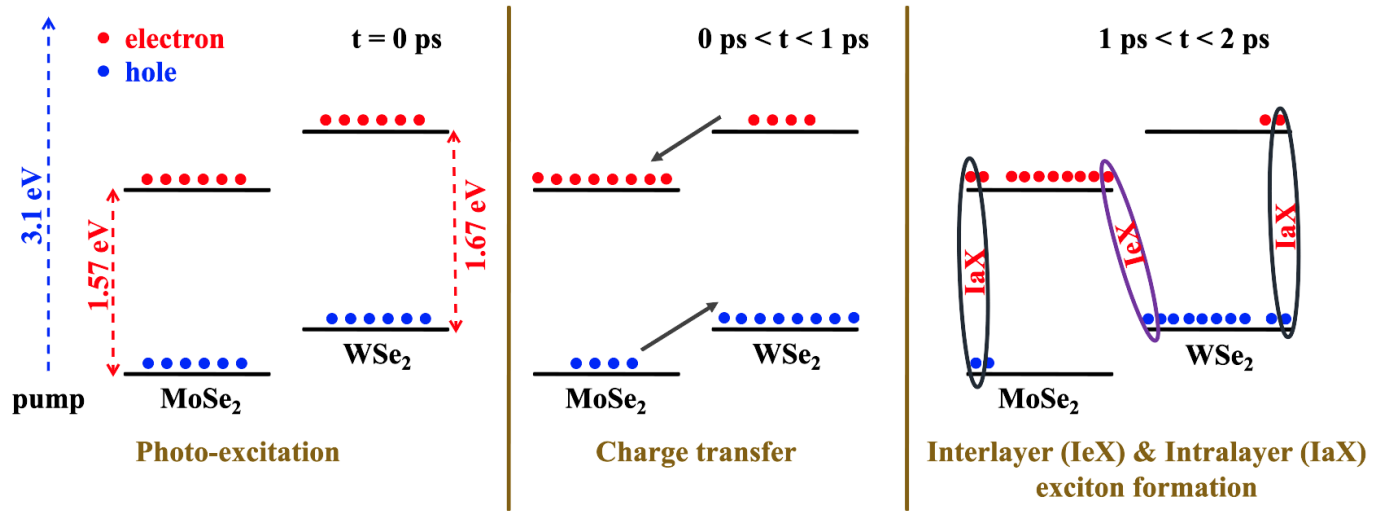


Figure 2: Type II band structure of HS MoSe₂/WSe₂, illustrating the charge transfer and the formation of the intralayer exciton (IaX) and interlayer exciton (IeX) at different time intervals after photoexcitation.

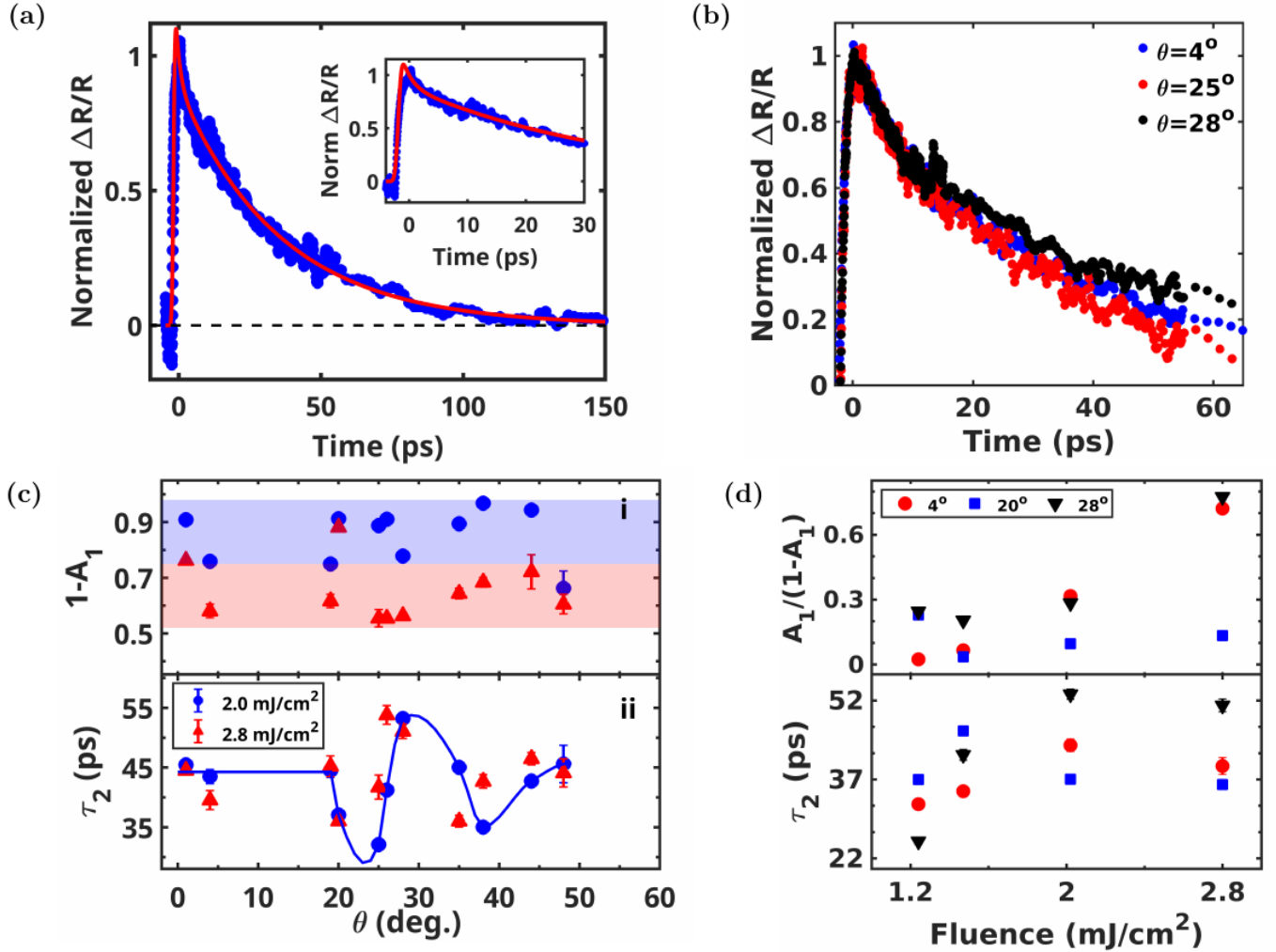


Figure 3: (a) Time evolution of normalized $\Delta R/R$ for MoSe₂/WSe₂ HS at a $\theta=20^\circ$, inset: the data up to 30 ps, the blue dots represent the data points and the red solid curve represents the fitting model given by Eq. 1, (b) The cumulative plot of normalized $\Delta R(t)/R$ emphasizes the twist angle (θ) dependence of the transient dynamics at a fluence of 2.0 mJ/cm^2 , (c) i. the fractional amplitude and ii. recombination time of interlayer excitons of HS at different twist angles for two different fluences (blue circle: $\phi_1=2.0 \text{ mJ/cm}^2$, red triangle: $\phi_2=2.8 \text{ mJ/cm}^2$). The solid blue line is a guide to the eye, (d) The fluence dependence of the fraction of intralayer to interlayer exciton density, and τ_2 for twist angles of 4° , 20° , and 28° .

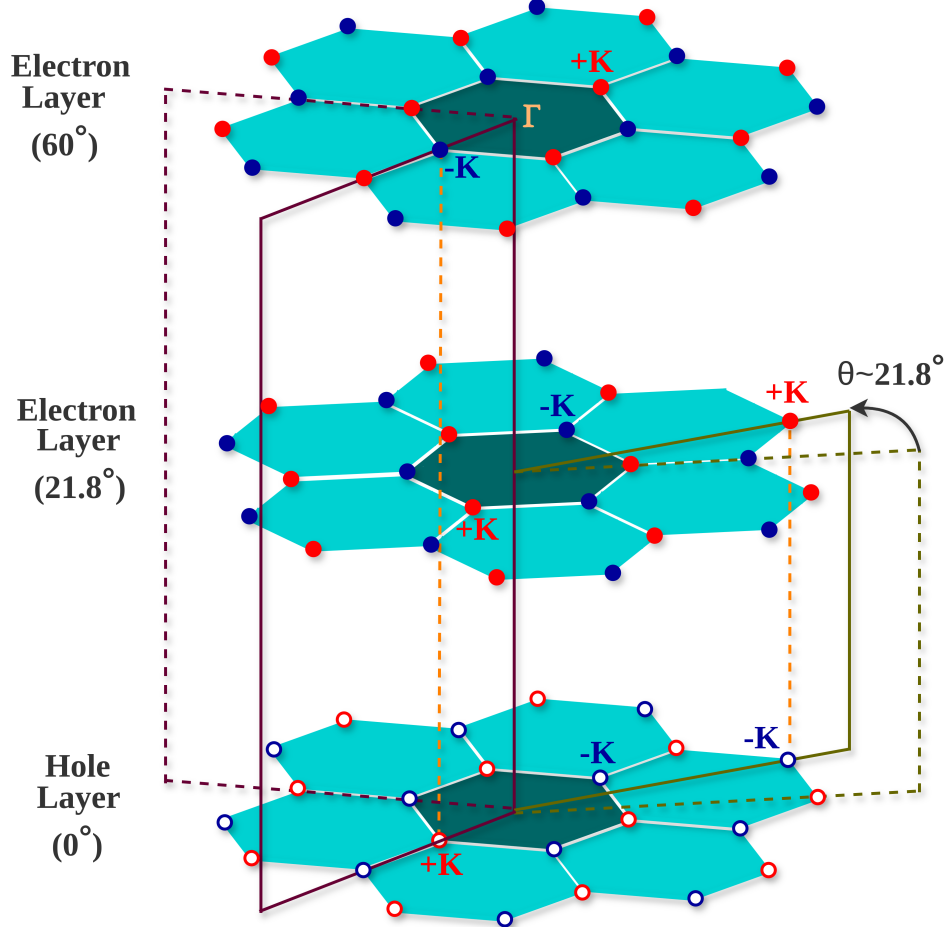


Figure 4: A schematic representation for the valley alignments in the extended Brillouin zone for a twisted HS: The solid and open dots represent the $-K$ (blue) and $+K$ (red) valleys in the electron and hole layers. For a twist angle of $\sim 21.8^\circ$, the valleys $+K$, $-K$ and $-K$, $+K$ align in the second Brillouin zone (indicated by an orange dashed line from the middle layer to the bottom layer), which has the same valley pairing for the 60° twisted HS (denoted by the orange dashed line from the top layer to the bottom layers). Consequently, the Umklapp process facilitates the recombination of interlayer excitons at commensurate twist angles. Adapted from *Seyler et al.* [26].

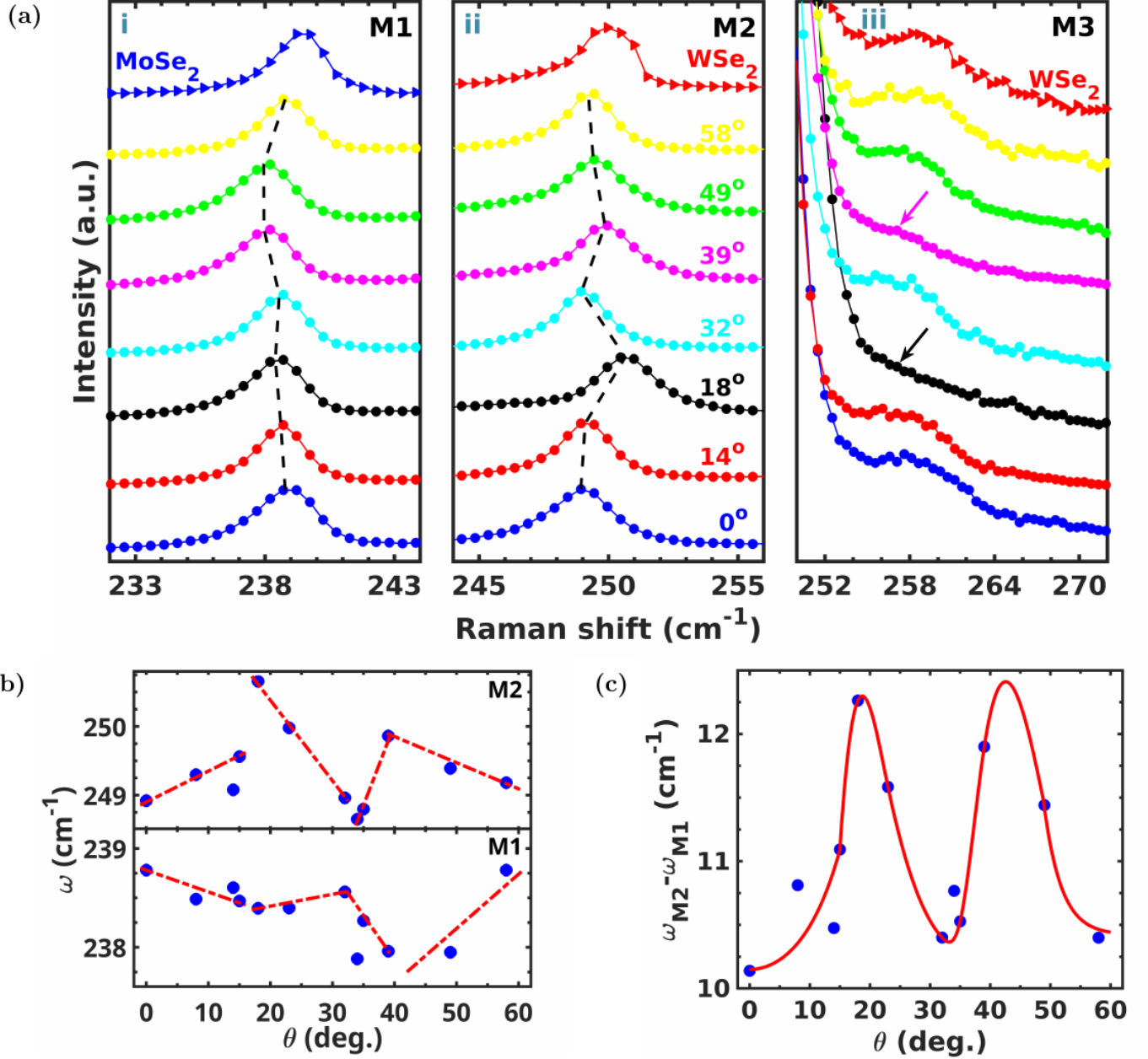


Figure 5: (a) The graphs depict i. M1, ii. M2 and iii. M3 modes at different twist angles and constituent monolayers. The corresponding stiffening and softening of M2 and M1, respectively, with the twist angle are indicated by the black dashed line, M3 mode disappears at $\theta=18^\circ$ and 39° as indicated by solid arrows in iii. (b) The frequency of M1 and M2 modes is plotted as a function of twist angle (θ), the dashed red lines represent the opposite trend of phonon frequencies of M1 and M2 modes with θ in the different twist regions, (c) The difference of frequencies of modes M1 and M2 is presented with twist angles. The difference is maximum in the proximity of commensurate angles of 21.8° and 38.2° .

References

- [1] Alexey Chernikov, Timothy C. Berkelbach, Heather M. Hill, Albert Rigosi, Yilei Li, Burak Aslan, David R. Reichman, Mark S. Hybertsen, and Tony F. Heinz. *Phys. Rev. Lett.*, **113**:076802, (2014).
- [2] Keliang He, Nardeep Kumar, Liang Zhao, Zefang Wang, Kin Fai Mak, Hui Zhao, and Jie Shan. *Phys. Rev. Lett.*, **113**:026803, (2014).
- [3] Yuanyuan Li, Qiannan Cui, Frank Ceballos, Samuel D. Lane, Zeming Qi, and Hui Zhao. *Nano Letters*, **17**(11):6661–6666, (2017).
- [4] Nardeep Kumar, Sina Najmaei, Qiannan Cui, Frank Ceballos, Pulickel M. Ajayan, Jun Lou, and Hui Zhao. *Phys. Rev. B*, **87**:161403, (2013).
- [5] Yilei Li, Yi Rao, Kin Fai Mak, Yumeng You, Shuyuan Wang, Cory R. Dean, and Tony F. Heinz. *Nano Letters*, **13**(7):3329–3333, (2013).
- [6] Leandro M. Malard, Thonimar V. Alencar, Ana Paula M. Barboza, Kin Fai Mak, and Ana M. de Paula. *Phys. Rev. B*, **87**:201401, (2013).
- [7] Hualing Zeng, Junfeng Dai, Wang Yao, Di Xiao, and Xiaodong Cui. *Nature Nanotechnology*, **7**:490–493, (2012).
- [8] Kin Fai Mak, Keliang He, Jie Shan, and Tony F. Heinz. *Nature Nanotechnology*, **7**:494–498, 2012.
- [9] Cheng Gong, Hengji Zhang, Weihua Wang, Luigi Colombo, Robert M. Wallace, and Kyeongjae Cho. *Applied Physics Letters*, **103**(5):053513, (2013).
- [10] Pramoda K. Nayak, Yevhen Horbatenko, Seongjoon Ahn, Gwangwoo Kim, Jae-Ung Lee, Kyung Yeol Ma, A-Rang Jang, Hyunseob Lim, Dogyeong Kim, Sunmin Ryu, Hyeonsik Cheong, Noejung Park, and Hyeon Suk Shin. *ACS Nano*, **11**(4):4041–4050, (2017).
- [11] Torben L. Purz, Eric W. Martin, Pasqual Rivera, William G. Holtzmann, Xiaodong Xu, and Steven T. Cundiff. *Phys. Rev. B*, **104**:L241302, (2021).
- [12] John R. Schaibley. In *OPTO*, (2017).
- [13] Yan Zeng, Wei Dai, Rundong Ma, Zhe Li, Zhenwei Ou, Cheng Wang, Yiling Yu, Tong Zhu, Xiaoze Liu, Ti Wang, and Hongxing Xu. *Small*, **18**(44):2204317, (2022).

- [14] Kha Tran, Galan Moody, Fengcheng Wu, Xiaobo Lu, Junho Choi, Kyounghwan Kim, Amritesh Rai, Daniel A. Sanchez, Jiamin Quan, Akshay Singh, Jacob Embley, André Zepeda, Marshall Campbell, Travis Autry, Takashi Taniguchi, Kenji Watanabe, Nanshu Lu, Sanjay K. Banerjee, Kevin L. Silverman, Suenne Kim, Emanuel Tutuc, Li Yang, Allan H. MacDonald, and Xiaoqin Li. *Nature*, **567**(7746):71–75, 2019.
- [15] Chenhao Jin, Emma C. Regan, Aiming Yan, M. Iqbal Bakti Utama, Danqing Wang, Sihan Zhao, Ying Qin, Sijie Yang, Zhiren Zheng, Shenyang Shi, Kenji Watanabe, Takashi Taniguchi, Sefaattin Tongay, Alex Zettl, and Feng Wang. *Nature*, **567**(7746):76–80, 2019.
- [16] James G. McHugh, Vladimir V. Enaldiev, and Vladimir I. Fal’ko. *Phys. Rev. B*, **108**:224111, Dec 2023.
- [17] Niclas Götting, Frederik Lohof, and Christopher Gies. *Phys. Rev. B*, **105**:165419, (2022).
- [18] Zidong Li, Xiaobo Lu, Darwin F. Cordovilla Leon, Zhengyang Lyu, Hongchao Xie, Jize Hou, Yanzhao Lu, Xiaoyu Guo, Austin Kaczmarek, Takashi Taniguchi, Kenji Watanabe, Liuyan Zhao, Li Yang, and Parag B. Deotare. *ACS Nano*, **15**(1):1539–1547, (2021).
- [19] Michael Förög, Anvar S. Baimuratov, Stanislav Yu. Kruchinin, Ilia A. Vovk, Johannes Scherzer, Jonathan Förste, Victor Funk, Kenji Watanabe, Takashi Taniguchi, and Alexander Högele. *Nature Communications*, **12**:1656, (2021).
- [20] Elena Blundo, Federico Tuzi, Salvatore Cianci, Marzia Cuccu, Katarzyna Olkowska-Pucko, Łucja Kipczak, Giorgio Contestabile, Antonio Miriametro, Marco Felici, Giorgio Pettinari, Takashi Taniguchi, Kenji Watanabe, Adam Babiński, Maciej R. Molas, and Antonio Polimeni. *Nature Communications*, **15**(1):1057, 2024.
- [21] V. V. Enaldiev, F. Ferreira, J. G. McHugh, and Vladimir I. Fal’ko. *npj 2D Materials and Applications*, **6**(1):74, 2022.
- [22] Long Zhang, Zhe Zhang, Fengcheng Wu, Danqing Wang, Rahul Gogna, Shaocong Hou, Kenji Watanabe, Takashi Taniguchi, Krishnamurthy Kulkarni, Thomas Kuo, Stephen R. Forrest, and Hui Deng. *Nature Communications*, **11**(1):5888, 2020.
- [23] Zhiming Zhang, Yimeng Wang, Kenji Watanabe, Takashi Taniguchi, Keiji Ueno, Emanuel Tutuc, and Brian J. LeRoy. *Nature Physics*, **16**(11):1093–1096, 2020.

[24] Trithep Devakul, Valentin Crépel, Yang Zhang, and Liang Fu. *Nature Communications*, **12**(1):6730, 2021.

[25] Kai Wang, Bing Huang, Mengkun Tian, Frank Ceballos, Ming-Wei Lin, Masoud Mahjouri-Samani, Abdelaziz Boulesbaa, Alexander A. Puretzky, Christopher M. Rouleau, Mina Yoon, Hui Zhao, Kai Xiao, Gerd Duscher, and David B. Geohegan. *ACS Nano*, **10**(7):6612–6622, (2016).

[26] Kyle L. Seyler, Pasqual Rivera, Hongyi Yu, Nathan P. Wilson, Essance L. Ray, David G. Mandrus, Jiaqiang Yan, Wang Yao, and Xiaodong Xu. *Nature*, **567**:66–70, (2019).

[27] Chirag Chandrakant Palekar, Joakim Hagel, Barbara Rosa, Samuel Brem, Ching-Wen Shih, Imad Limame, Martin von Helversen, Sefaattin Tongay, Ermin Malic, and Stephan Reitzenstein. *2D Materials*, **11**(2):025034, 2024.

[28] Nikodem Sokolowski, Swaroop Palai, Mateusz Dyksik, Katarzyna Posmyk, Michał Baranowski, Alessandro Surrente, Duncan Maude, Felix Carrascoso, Onur Cakiroglu, Estrella Sanchez, Alina Schubert, Carmen Munuera, Takashi Taniguchi, Kenji Watanabe, Joakim Hagel, Samuel Brem, Andres Castellanos-Gomez, Ermin Malic, and Paulina Plochocka. *2D Materials*, **10**(3):034003, 2023.

[29] Ke Wu, Hongxia Zhong, Quanbing Guo, Jibo Tang, Jing Zhang, Lihua Qian, Zhifeng Shi, Chendong Zhang, Shengjun Yuan, Shunping Zhang, and Hongxing Xu. *National Science Review*, **9**, (2021).

[30] Lishu Wu, Chunxiao Cong, Jingzhi Shang, Weihuang Yang, Yu Chen, Jiadong Zhou, Wei Ai, Yanlong Wang, Shun Feng, Hongbo Zhang, Zheng Liu, and Ting Yu. *Nano Research*, **14**:2215–2223, (2021).

[31] Hongyi Yu, Yong Wang, Qingjun Tong, Xiaodong Xu, and Wang Yao. *Phys. Rev. Lett.*, **115**:187002, (2015).

[32] Hanping Xiong, Xianhua Nie, Li Zhao, and Shuai Deng. *ACS Applied Materials & Interfaces*, **16**(19):25124–25135, 2024. PMID: 38709893.

[33] Saurav Sachin, Puja Kumari, Neelam Gupta, Shivani Rani, Subhasmita Kar, and Soumya Jyoti Ray. *Computational Condensed Matter*, **35**:e00797, 2023.

[34] Soo Yeon Lim, Han-gyu Kim, Young Woo Choi, Takashi Taniguchi, Kenji Watanabe, Hyoung Joon Choi, and Hyeonsik Cheong. *ACS Nano*, **17**(14):13938–13947, 2023. PMID: 37410957.

[35] Ziheng Ji, Hao Hong, Jin Zhang, Qi Zhang, Wei Huang, Ting Cao, Ruixi Qiao, Can Liu, Jing Liang, Chuanhong Jin, Liying Jiao, Kebin Shi, Sheng Meng, and Kaihui Liu. *ACS Nano*, **11**(12):12020–12026, (2017).

[36] Amalya C. Johnson, Johnathan D. Georgaras, Xiaozhe Shen, Helen Yao, Ashley P. Saunders, Helen J. Zeng, Hyungjin Kim, Aditya Sood, Tony F. Heinz, Aaron M. Lindenberg, Duan Luo, Felipe H. da Jornada, and Fang Liu. *Science Advances*, **10**(4):eadj8819, 2024.

[37] Xiaoping Hong, Jonghwan Kim, Su-Fei Shi, Yu Zhang, Chenhao Jin, Yinghui Sun, Sefaattin Tongay, Junqiao Wu, Yanfeng Zhang, and Feng Wang. *Nature Nanotechnology*, **9**(9):682–686, (2014).

[38] Frank Ceballos, Matthew Z. Bellus, Hsin-Ying Chiu, and Hui Zhao. *ACS Nano*, **8**(12):12717–12724, (2014).

[39] Frank Ceballos, Matthew Z. Bellus, Hsin-Ying Chiu, and Hui Zhao. *Nanoscale*, **7**:17523–17528, (2015).

[40] Bo Peng, Yu Guannan, Liu Xinfeng, Bo Liu, Xiao Liang, Lei Bi, Longjiang Deng, Tze Chien Sum, and Kian Ping Loh. *2D Materials*, **3**(2):025020, (2016).

[41] Peymon Zereshki, Yaqing Wei, Run Long, and Hui Zhao. *The Journal of Physical Chemistry Letters*, **9**(20):5970–5978, (2018).

[42] R. Krause, S. Aeschlimann, M. Chávez-Cervantes, R. Pereira-Causin, S. Brem, E. Malic, S. Forti, F. Fabbri, C. Coletti, and I. Gierz. *Phys. Rev. Lett.*, **127**:276401, (2021).

[43] Jin Zhang, Hao Hong, Chao Lian, Wei Ma, Xiaozhi Xu, Xu Zhou, Huixia Fu, Kaihui Liu, and Sheng Meng. *Advanced Science*, **4**(9):1700086, (2017).

[44] Albert F. Rigosi, Heather M. Hill, Yilei Li, Alexey Chernikov, and Tony F. Heinz. *Nano Letters*, **15**(8):5033–5038, (2015).

[45] Yuan Liu, Nathan O. Weiss, Xidong Duan, Hung-Chieh Cheng, Yu Huang, and Xiangfeng Duan. *Nature Reviews Materials*, **1**(9):16042, (2016).

[46] A M van der Zande, P Y Huang, D A Chenet, T C Berkelbach, Y You, G H Lee, T F Heinz, D R Reichman, D A Muller, and J C Hone. *Nature materials*, **12**:554–561, (2013).

[47] Jeppe V. Lauritsen, Jakob Kibsgaard, Stig Helveg, Henrik Topsøe, Bjerne S. Clausen, Erik Lægsgaard, and Flemming Besenbacher. *Nature Nanotechnology*, **2**(1):53–58, (2007).

[48] Xu Zhou, Jingxin Cheng, Yubing Zhou, Ting Cao, Hao Hong, Zhimin Liao, Shiwei Wu, Hailin Peng, Kaihui Liu, and Dapeng Yu. *Journal of the American Chemical Society*, **137**(25):7994–7997, (2015).

[49] Kaihui Liu, Liming Zhang, Ting Cao, Chenhao Jin, Diana Qiu, Qin Zhou, Alex Zettl, Peidong Yang, Steve G. Louie, and Feng Wang. *Nature Communications*, **5**:4966, (2014).

[50] Xin Lu, M. Iqbal Bakti Utama, Junhao Lin, Xue Gong, Jun Zhang, Yanyuan Zhao, Sokrates T. Pantelides, Jingxian Wang, Zhili Dong, Zheng Liu, Wu Zhou, and Qihua Xiong. *Nano Letters*, **14**(5):2419–2425, 2014.

[51] Jing-Kai Huang, Jiang Pu, Chang-Lung Hsu, Ming-Hui Chiu, Zhen-Yu Juang, Yung-Huang Chang, Wen-Hao Chang, Yoshihiro Iwasa, Taishi Takenobu, and Lain-Jong Li. *ACS Nano*, **8**(1):923–930, 2014.

[52] Ying Jiang, Shula Chen, Weihao Zheng, Biyuan Zheng, and Anlian Pan. *Light: Science & Applications*, **10**(1):72, 2021.

[53] Hoseok Heo, Ji Ho Sung, Soonyoung Cha, Bo-Gyu Jang, Joo-Youn Kim, Gangtae Jin, Donghun Lee, Ji-Hoon Ahn, Myoung-Jae Lee, Ji Hoon Shim, Hyunyong Choi, and Moon-Ho Jo. *Nature Communications*, **6**(1):7372, 2015.

[54] Mei Yang, Xuerui Cheng, Yuanyuan Li, Yufen Ren, Miao Liu, and Zeming Qi. *Applied Physics Letters*, **110**(9):093108, (2017).

[55] Woosuk Choi, Imtisal Akhtar, Malik Abdul Rehman, Minwook Kim, Dongwoon Kang, Jongwan Jung, Yoon Myung, Jungcheol Kim, Hyeonsik Cheong, and Yongho Seo. *ACS Applied Materials & Interfaces*, **11**(2):2470–2478, (2019).

[56] Lama Khalil, Debora Pierucci, Emilio Velez-Fort, José Avila, Céline Vergnaud, and Pavel Dudin. *Nanotechnology*, **34**:045702, (2023).

[57] Xin Zhang, Xiao-Fen Qiao, Wei Shi, Jiang-Bin Wu, De-Sheng Jiang, and Ping-Heng Tan. *Chem. Soc. Rev.*, **44**:2757–2785, (2015).

- [58] Biswanath Chakraborty, Achintya Bera, D. V. S. Muthu, Somnath Bhowmick, U. V. Waghmare, and A. K. Sood. *Phys. Rev. B*, **85**:161403, (2012).
- [59] Changgu Lee, Hugen Yan, Louis E. Brus, Tony F. Heinz, James Hone, and Sunmin Ryu. *ACS Nano*, **4**(5):2695–2700, 2010.
- [60] A. Molina-Sánchez and L. Wirtz. *Phys. Rev. B*, **84**:155413, 2011.